Design of Hierarchical Core−Corona Architectures of Layered Manganese Oxides by Aqueous Precipitation

David Portehault,[†,‡] Sophie Cassaignon,*[,†,‡] Emmanuel Baudrin,[§] and Jean-Pierre Jolivet[†,‡]

UPMC Univ Paris 06, UMR 7574, Chimie de la Matière Condensée de Paris, cc 174, 4 place Jussieu, F-75005 Paris, France, CNRS, UMR 7574, Chimie de la Matière Condensée de Paris, cc 174, 4 place Jussieu, F-75005 Paris, France, Université de Picardie-Jules Verne, UMR 6007, Laboratoire de Réactivité et Chimie des Solides, 33 rue Saint-Leu, 80039 Amiens cedex, France

Received May 22, 2008. Revised Manuscript Received July 23, 2008

A low temperature (60 or 95 °C), "one-pot" procedure for aqueous precipitation of layered manganese oxide core@shell particles is developed, based on the reaction between MnO_4^- and Mn^{2+}. Characterization of the particles was carried out using powder XRD, nitrogen adsorption−desorption, FESEM, TEM, and electron diffraction. Textural and morphological tailoring is achieved through various experimental parameters, with the specific surface area adjusted between 15 and 110 $m^2\ g^{-1}$ while a ball-like or sheetlike shape is selectively obtained. The synthesis is based on a two-step precipitation process, with the first stage involving in situ seeding and enabling shape control via adjustment of the initial acidity. Hierarchical core−corona particles are obtained through a second slower heterogeneous nucleation stage, controlled by reactant ratio, aging time, temperature, and acidity of the aging medium.

Introduction

Nanotextured materials nowadays attract interest due to unique properties.[1] Actually, the shape and the size of nanoscaled materials have been shown to greatly influence many properties in various domains such as electrochemistry, catalysis or optics.[1] To tune these properties, a great number of research works are oriented toward size, morphology, and texture control. Moreover, a growing number of studies is now dedicated to ordering nanodomains within the material at the mesoscale.[2−13] Control of such complex architectures has been explored especially through nanoparticle assemblies.[6−13] Nevertheless, tuning self-assembly processes is still difficult to achieve and usually requires organic solvents and/or templates such as surfactants, implying costly purification processes and detrimental environmental impact.[1,4−6,12,13] Another way to attain hierarchical ordering in terms of structure and morphology is to tune heterogeneous nucleation processes. This has been demonstrated particularly through the design of various core@shell architectures.[14−24] However, reported synthetic procedures are often limited to the synthesis of inorganic@organic particles.[15−18] When fully inorganic structures are needed, processes implying two subsequent precipitation steps are commonly used, for core precipitation followed by shell growth, despite the cost of necessary intermediate purifications.[14,25] "One-pot" procedures are much scarcer because they require decorrelating core and shell formation.[19−21,25−30] The next step toward controlled behaviors in various fields such as catalysis and

* To whom correspondence should be addressed. E-mail: sophie.cassaignon@upmc.fr.
† UPMC Univ Paris 06.
‡ CNRS, UMR 7574.
§ Université de Picardie-Jules Verne.

(1) Burda, C.; Chen, X.; Narayanan, R.; El-Sayed, M. A. *Chem. Rev.* **2005**, *105*, 1025–1102.
(2) Alivisatos, A. P. *Science* **1996**, *271*, 933–937.
(3) Bezryadin, A.; Lau, C. N.; Tinkham, M. *Nature* **2000**, *404*, 971–974.
(4) Cölfen, H.; Antonietti, M. *Angew. Chem., Int. Ed.* **2005**, *44*, 5576–5591.
(5) Tian, Z. R.; Voigt, J. A.; Liu, J.; Mckenzie, B.; Mcdermott, M. J.; Rodriguez, M. A.; Konishi, H.; Xu, H. *Nat. Mater.* **2003**, *2*, 821–826.
(6) Garnweitner, G.; Niederberger, M. *J. Mater. Chem.* **2008**, *18*, 1171–1182.
(7) Niederberger, M.; Cölfen, H. *Phys. Chem. Chem. Phys.* **2006**, *8*, 3271–3287.
(8) Cho, K.-S.; Talapin, D. V.; Gaschler, W.; Murray, C. B. *J. Am. Chem. Soc.* **2005**, *127*, 7140–7147.
(9) Cölfen, H.; Mann, S. *Angew. Chem., Int. Ed.* **2003**, *42*, 2350–2365.
(10) Antonietti, M.; Niederberger, M.; Smarsly, B. *Dalton Trans.* **2008**, 18–24.
(11) Shevchenko, E. V.; Ringler, M.; Schwemer, A.; Talapin, D. V.; Klar, T. A.; Rogach, A. L.; Feldmann, J.; Alivisatos, A. P. *J. Am. Chem. Soc.* **2008**, *130*, 3274–3275.
(12) Mokari, T.; Zhang, M.; Yang, P. *J. Am. Chem. Soc.* **2007**, *129*, 9864–9865.
(13) Tao, A. R.; Habas, S.; Yang, P. *Small* **2008**, *4*, 310–325.
(14) Habas, S. E.; Lee, H.; Radmilovic, V.; Somorjai, G. A.; Yang, P. *Nat. Mater.* **2007**, *6*, 692–697.
(15) Sacanna, S.; Philipse, A. P. *Adv. Mater.* **2007**, *19*, 3824–3826.
(16) Cheng, D.; Zhou, X.; Xia, H.; Chan, H. S. O. *Chem. Mater.* **2005**, *17*, 3578–3581.
(17) Choi, W. S.; Koo, H. Y.; Huck, W. T. S. *J. Mater. Chem.* **2007**, *17*, 4943–4946.
(18) Shi, Q.; An, Z.; Tsung, C.-K.; Liang, H.; Zheng, N.; Hawker, C. J.; Stucky, G. D. *Adv. Mater.* **2007**, *19*, 4539–4543.
(19) Du, J.; Zhang, J.; Liu, Z.; Han, B.; Jiang, T.; Huang, Y. *Langmuir* **2006**, *22*, 1307–1312.
(20) Pastoriza-Santos, I.; Koktysh, D. S.; Mamedov, A. A.; Giersig, M.; Kotov, N. A.; Liz-Marzan, L. M. *Langmuir* **2000**, *16*, 2731–2735.
(21) Sun, X. M.; Li, Y. D. *Langmuir* **2005**, *21*, 6019–6024.
(22) Camargo, P. H. C.; Lee, Y. H.; Jeong, U.; Zou, Z.; Xia, Y. *Langmuir* **2007**, *23*, 2985–2992.
(23) Ge, J.; Hu, Y.; Zhang, T.; Yin, Y. *J. Am. Chem. Soc.* **2007**, *129*, 8974–8975.
(24) DiMaio, J. R.; Kokuoz, B.; James, T.; Ballato, J. *Adv. Mater.* **2007**, *19*, 3266–3270.
(25) Liz-Marzan, L. M.; Mulvaney, P. *J. Phys. Chem. B* **2003**, *107*, 7312–7326.
(26) Li, Z.; Ding, Y.; Xiong, Y.; Yang, Q.; Xie, Y. *Chem. Commun.* **2005**, 918–920.
(27) Rao, C. N. R.; Vivekchand, S. R. C.; Biswas, K.; Govindaraj, A. *Dalton Trans.* **2007**, 3728–3749.

10.1021/cm801400b CCC: $40.75
Published on Web 09/23/2008

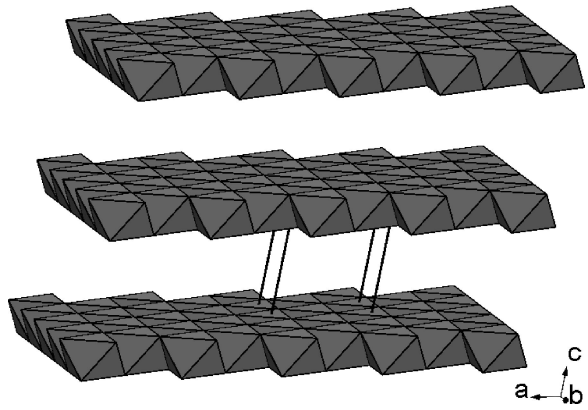

Figure 1. Idealized crystalline framework of K-birnessite layered manganese oxide (b-LMO). K^+ and H_2O interlayer species are not shown.

energy storage is the development of simple procedures that provide versatile and easy tailoring of shape, size, and texture of core@shell architectures. However, to the best of our knowledge, none of the already reported studies demonstrated the efficiency of "one-pot" approaches for such control. Therefore, the elaboration of "one-pot" and versatile syntheses of core@shell particles still remains a great challenge. Moreover, the development of environmentally friendly and template free procedures could increase the viability of such materials.

Birnessite is one class of intercalation compounds among the numerous manganese oxide MnO_2 polymorphs.[31] This allotrope has mixed valence (III, IV), and its idealized structure is characterized by a lamellar framework made of MnO_6 octahedra layers (Figure 1).[31,32] Usually, some defects are observed in the layers such as vacancies, Mn^{4+} substitution by Mn^{3+}, or Mn^{4+} migration in the interlayer.[33−36] As a consequence, the octahedra layers have a negative charge which is compensated by intercalation in the interlayer of various cations such as alkaline (K^+, Na^+, or Li^+),[37,38] akaline-earth (Mg^{2+}),[37] (tetraalkyl)ammonium,[39]together with water molecules. Birnessite-type layered manganese oxides (b-LMO) compounds are intensively studied because of their exchange properties[38] and energy storage applications as electrode materials for Li batteries[40−44] or supercondensators.[45,46]

Birnessite is also a solid precursor to many other manganese oxides.[47,48] Synthesis of such materials usually occur in aqueous medium, under thermal[49−52] or hydrothermal[45] conditions, using sol−gel[49,53,54] or precipitation[51,52] methods. These procedures imply the use of a soluble Mn precursor and an adequate redox agent: for instance Mn^{2+} oxidation by H_2O_2,[38] MnO_4^- reduction by sugars[53,54] or alcohols,[55] Mn^{2+}/MnO_4^- reaction.[45] Shapes resulting from these routes are usually submicro- or nanosheets.[52,56,57] Few studies report on the synthesis of nanobelts,[58−60] whereas more complex structures have been obtained by Yan et al. and Hill et al., who reported the synthesis of flowerlike particles.[61,62] Recently, our group has demonstrated that spherical core−corona b-LMO architectures could be obtained using a "one-pot" synthesis under soft conditions in aqueous medium, with a two-step precipitation involving in situ seeding and subsequent heterogeneous nucleation.[30] Taking advantage of the various morphologies already obtained for birnessite-type layered manganese oxides, it could be possible to improve shape and texture control of core@shell particles, thus providing efficient means for property tailoring.

Herein is reported a low-emperature (60−95 °C) synthesis of potassium intercalated b-LMO by aqueous precipitation. The scope of this study is to demonstrate the achievable structure, shape, and texture control of core−corona b-LMO particles by highlighting the key experimental parameters that act upon the precipitation processes. These are discussed according to a formation mechanism that was previously reported.[30]

(28) Tom, R. T.; Nair, A. S.; Singh, N.; Aslam, M.; Nagendra, C. L.; Philip, R.; Vijayamohanan, K.; Pradeep, T. *Langmuir* **2003**, *19*, 3439–3445.
(29) Lai, J.; Shafi, K. V. P. M.; Ulman, A.; Loos, K.; Popovitz-Biro, R.; Lee, Y.; Vogt, T.; Estournes, C. *J. Am. Chem. Soc.* **2005**, *127*, 5730–5731.
(30) Portehault, D.; Cassaignon, S.; Nassif, N.; Baudrin, E.; Jolivet, J.-P. *Angew. Chem., Int. Ed.* **2008**, *47*, 6441–6444.
(31) Post, J. E. *Proc. Natl. Acad. Sci. U.S.A.* **1999**, *96*, 3447–3454.
(32) Chen, R.; Zavalij, P.; Whittingham, M. S. *Chem. Mater.* **1996**, *8*, 1275–1280.
(33) Giovanoli, R.; Buerki, P.; Giuffredi, M.; Stumm, W. *Chimia* **1975**, *29*, 517–520.
(34) Gaillot, A.-C.; Flot, D.; Drits, V. A.; Manceau, A.; Burghammer, M.; Lanson, B. *Chem. Mater.* **2003**, *15*, 4666–4678.
(35) Gaillot, A.-C.; Lanson, B.; Drits, V. A. *Chem. Mater.* **2005**, *17*, 2959–2975.
(36) Gaillot, A.-C.; Drits, V. A.; Manceau, A.; Lanson, B. *Microporous Mesoporous Mater.* **2007**, *98*, 267–282.
(37) Post, J. E.; Veblen, D. R. *Am. Mineral.* **1990**, *75*, 477–489.
(38) Prieto, O.; Arco, M. D.; Rives, V. *J. Mater. Sci.* **2003**, *38*, 2815–2824.
(39) Luo, J.; Suib, S. L. *Chem. Commun.* **1997**, *11*, 1031–1032.
(40) Bach, S.; Pereira-Ramos, J. P.; Baffier, N. *J. Solid State Chem.* **1995**, *120*, 70–73.
(41) Bach, S.; Pereira-Ramos, J. P.; Baffier, N.; Messina, R. *Electrochim. Acta* **1991**, *36*, 1595–1603.
(42) Yagi, H.; Ichikawa, T.; Hirano, A.; Imanishi, N.; Ogawa, S.; Takeda, Y. *Solid State Ionics* **2002**, *154−155*, 273–278.
(43) Bach, S.; Pereira-Ramos, J. P.; Baffier, N. *Electrochim. Acta* **1993**, *38*, 1695–1698.
(44) Thackeray, M. M. *Prog. Solid State Chem.* **1997**, *25*, 1.
(45) Subramanian, V.; Zhu, H.; Vajtai, R.; Ajayan, P. M.; Wei, B. *J. Phys. Chem. B* **2005**, *109*, 20207–20214.
(46) Brousse, T.; Toupin, M.; Dugas, R.; Athouel, L.; Crosnier, O.; Belanger, D. *J. Electrochem. Soc.* **2006**, *153*, A2171−A2180.
(47) Chen, C. C.; Golden, D. C.; Dixon, J. B. *Clays Clay Miner.* **1986**, *34*, 565–571.
(48) Shen, Y. F.; Zerger, R. P.; DeGuzman, R. N.; Suib, S. L.; McCurdy, L.; Potter, D. I.; O'Young, C.-L. *Science* **1993**, *260*, 511–515.
(49) Luo, J.; Suib, S. L. *J. Phys. Chem. B* **1997**, *101*, 10403–10413.
(50) Yang, D. S.; Wang, M. K. *Chem. Mater.* **2001**, *13*, 2589–2594.
(51) Ma, Y.; Luo, J.; Suib, S. L. *Chem. Mater.* **1999**, *11*, 1972–1979.
(52) Luo, J.; Huang, A.; Park, S. H.; Suib, S. L.; O'Young, C.-L. *Chem. Mater.* **1998**, *10*, 1561–1568.
(53) Ching, S.; Landigran, J. A.; Jorgensen, M. L.; Duan, N.; Suib, S. L.; O'Young, C. L. *Chem. Mater.* **1995**, *7*, 1604–1606.
(54) Ching, S.; Petrovay, D. J.; Jorgensen, M. L.; Suib, S. L. *Inorg. Chem.* **1997**, *36*, 883–890.
(55) Brock, S. L.; Sanabria, M.; Suib, S. L.; Urban, V.; Thiyagarajan, P.; Potter, D. I. *J. Phys. Chem. B* **1999**, *103*, 7416–7428.
(56) Omomo, Y.; Sasaki, T.; Wang, L. Z.; Watanabe, M. *J. Am. Chem. Soc.* **2003**, *125*, 3568–3575.
(57) Oaki, Y.; Imai, H. *Angew. Chem., Int. Ed.* **2007**, *46*, 4951–4955.
(58) Ma, R.; Bando, Y.; Zhang, L.; Sasaki, L. *Adv. Mater.* **2004**, *16*, 918–922.
(59) Zhang, H. T.; Chen, X. H.; Zhang, J. H.; Wang, G. Y.; Zhang, S. Y.; Long, Y. Z.; Chen, Z. J.; Wang, N. L. *J. Cryst. Growth* **2005**, *280*, 292–299.
(60) Liu, Z.; Ma, R.; Ebina, Y.; Takada, K.; Sasaki, T. *Chem. Mater.* **2007**, *19*, 6504–6512.
(61) Yan, D.; Yan, P. X.; Yue, G. H.; Liu, J. Z.; Chang, J. B.; Yang, Q.; Qu, D. M.; Geng, Z. R.; Chen, J. T.; Zhang, G. A.; Zhuo, R. F. *Chem. Phys. Lett.* **2007**, *440*, 134–138.
(62) Hill, J. P.; Alam, S.; Ariga, K.; Anson, C. E.; Powell, A. K. *Chem. Commun.* **2008**, 383–385.

Table 1

sample name	initial Mn^{VII}:Mn^{II} ratio	*T* (°C)	aging duration (days)	AOS[a]	K:Mn[b]	morphology	dimensions (nm)
S60	2:3	60	7	3.53	0.15	sheets	10 × 300
S95	2:3	95	7	3.64	0.15	sheets	10 × 300
E60	20:3	60	7	3.76	0.17	sheets	20 × 300
E95	20:3	95	7	3.59	0.17	core−corona sheets	30 × 300
A60	20:3	60	7	3.74	0.19	spongelike core−corona balls	400 (diameter)
A95[c]	20:3	95	7	3.68	0.19	spongelike core−corona balls	400 (diameter)

[a] Average oxidation state. [b] K:Mn molar ratio of birnessite samples. [c] The **A95** sample has been described previously.[30]

Experimental Section

Synthesis. Birnessite has been synthesized using reaction between Mn^{2+} and MnO_4^- in water with total Mn concentration of 0.2 mol L^{-1}. To investigate the influence of the reactant ratio, we used two procedures, depending on the initial Mn^{VII}:Mn^{II} ratio.

Mn^{VII}:Mn^{II} = 2:3. The Mn^{VII}:Mn^{II} ratio corresponds to the stoichiometry of the following equation

$$2MnO_4^- + 3Mn^{2+} + 2H_2O \rightarrow 5MnO_2 + 4H^+ \qquad (1)$$

After nitrogen bubbling for 30 min, the pH of a $MnSO_4$, H_2O aqueous solution (75 mL, 30 mmol, Aldrich) was adjusted to 11 by addition of a ca. 2 mol L^{-1} KOH solution under nitrogen bubbling. The white solid $Mn(OH)_2$ precipitated immediately. A $KMnO_4$ solution (150 mL, 20 mmol, Aldrich) at pH 11 was then added to the $Mn(OH)_2$ dispersion under vigorous stirring and nitrogen bubbling. The adding rate was 1.25 mL s^{-1} and mixing was completed after 2 min. The volume was adjusted to 250 mL with an aqueous solution at pH 11. The white precipitate turned black immediately.

Mn^{VII}:Mn^{II} = 20:3. Synthesis were performed using the same procedure as the 2:3 ratio, except that the Mn^{VII}:Mn^{II} ratio was 20:3 with 200 mL of $KMnO_4$ solution (43 mmol, Aldrich) and 30 mL of $MnSO_4$,H_2O solution (7.0 mmol, Aldrich). Acidity was adjusted at pH 11 as described for the 2:3 ratio. For comparison of the textural properties, spongelike particles of b-LMO have been synthesized using the same procedure, but at initial pH 2 as described previously.[30]

For both procedures, suspensions were aged in an oven at 25, 60, or 95 °C for 7 days and shaken once per day. Samples were collected at different times (on a duration of 7 days) and centrifuged. The powders were washed three times with deionized water and first dried at room temperature under nitrogen flux. They were then dried in an oven at 95 °C overnight. The reaction is quantitative and yields approximately 4 g of solid. Samples obtained after aging 7 days at 60 or 95 °C are named, respectively, **S60** and **S95** for Mn^{VII}:Mn^{II} ratio 2:3 and **E60**, **E95** for ratio 20:3 (Table 1). Samples obtained using ratio 20:3 at initial pH 2 are referred to as **A60** and **A95**.[30]

Techniques. *MnO_4^- and Mn^{2+} Titration.* Linear scan hydrodynamic voltammetry was used to titrate the supernatant. The procedure has been described previously.[63] A rotating platinum disk was used as the working electrode, a saturated calomel electrode (SCE) as reference and platinum as counter electrode. Rotation speed was 400 rpm. Analyzed solutions were diluted ten times in the supporting electrolyte solution (HNO_3 1 mol L^{-1}) saturated with argon bubbling. Two linear scans at 10 mV s^{-1} sweep rate were carried out from 0.5 to 1.5 V vs SCE and from 1.4 to 0.7 V to determine Mn^{2+} and MnO_4^- concentrations, respectively. Limiting currents were measured and concentrations were evaluated from calibration curves (I_l (A) = 1.86 × 10^{-1} [Mn^{2+}] (mol L^{-1}) and I_l (A) = 6.34 × 10^{-2} [MnO_4^-] (mol L^{-1}), respectively).

Mn Average Oxidation State (AOS) Determination. The AOS was determined using a two-step procedure described previously.[63] The particles were dissolved in a H_2SO_4 solution, whereas Mn^{III} and Mn^{IV} were reduced to soluble Mn^{II} using Fe^{2+}. Titrations of the resulting Mn^{2+} and the excess of Fe^{2+} enabled to determine the AOS. The relative error is evaluated to 5%.

Elemental Analysis. K and Mn elemental ratios were determined at the CNRS Service Central d'Analyze, USR 59. Both AOS determination and elemental analysis enabled the determination of K and Mn compositions.

X-Ray Diffraction (XRD). Powder XRD measurements were performed with a Brücker D8 X-ray diffractometer operating in the reflection mode at Cu *K*α radiation with 40 kV beam voltage and 40 mA beam current. The data were collected in the 8−70° range (2θ) with steps of 0.05° and a counting time of 14 s. XRD patterns were indexed using the monoclinic structure of birnessite.[64] Crystallite apparent mean size was determined using the Scherrer equation with the integral breadths corrected for the instrumental broadening. The (001) peak of birnessite was exploited.

N_2 Adsorption−desorption. Textural properties were investigated using an ASAP 2010 Micrometrics apparatus. Adsorption and desorption of N_2 were performed at 77 K. Specific surface areas (S_{BET}) were determined following the BET analysis. α-Plots were drawn using a macroporous β-MnO_2 allotrope reference sample. Samples had been previously outgassed by heating at 120 °C overnight under a 3 μm Hg pressure.

Field-Emission Scanning Electron Microscopy (FESEM). FESEM observations and energy-dispersive X-ray analysis (EDX) have been performed using an Hitachi apparatus (2 kV) equipped with an Oxford analyzer.

Transmission Electron Microscopy (TEM). The nanoparticle morphology and orientation were studied by TEM and selected area electron diffraction (SAED) using a JEOL 100CX (100 kV) apparatus, and high-resolution TEM (HRTEM) using a Philips CM20 (200 kV) apparatus. Samples were prepared by evaporating a drop of aqueous diluted suspension on a carbon-coated copper grid. The *d*-spacings obtained from SAED patterns were calibrated using Au pattern. When particles were too thick for direct HRTEM study under a selected direction, ultra thin sections were carried out by embedding the sample in an epoxy resin. The cutting of the block was performed using an ultra microtome (Ultracut Reichert Jung). Thickness of the sections is ca.70 nm.

Results

Birnessite has been synthesized using reaction between MnO_4^- and Mn^{2+} in water. At initial pH 11, and for both Mn^{VII}:Mn^{II} ratios (20:3 and 2:3), a solid precipitates when elevating the pH of the $MnSO_4$ solution above 8 before the

(63) Portehault, D.; Cassaignon, S.; Baudrin, E.; Jolivet, J.-P. *Chem. Mater.* **2007**, *19*, 5410–5417.

(64) JCPDS file 42−1348.

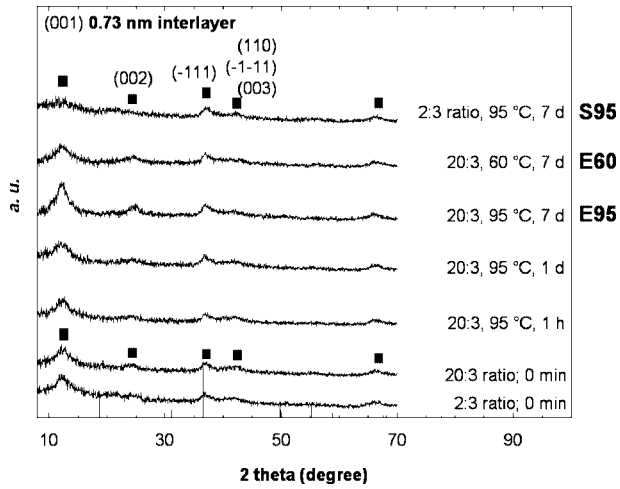

Figure 2. Powder XRD patterns of K-birnessite layered manganese oxide (b-LMO) samples (■) obtained after different aging times for the 2:3 and 20:3 Mn^{VII}:Mn^{II} ratios. Reference pattern of pyrochroite (—).[65]

reactant mixing. The white color of this compound spontaneously turns into brown over air exposure, revealing oxidation and structure modification. Therefore, XRD cannot be performed on the initial solid. Nevertheless, its white color is unique among the manganese (oxihydr)oxides and is characteristic of the layered $Mn(OH)_2$ pyrochroite compound. The mixture darkens when the $KMnO_4$ solution is added. Powder XRD patterns (Figure 2) indicate that birnessite is immediately obtained. The distance range of ordered stacking between MnO_6 layers evaluated from the (001) peak of the XRD patterns for the powders obtained with the 20:3 ratio after 7 days of aging is ca. 9 nm at 95 °C (sample **E95**) and 7 nm at 60 °C (sample **E60**).

The supernatant pH obtained after few days of aging is approximately 12 for all the samples. Electrochemical characterization of the supernatant shows that the whole Mn^{2+} quantity initially present in solution has reacted after one hour. Concerning the consumption of $KMnO_4$, two different behaviors are observed depending on the initial Mn^{VII}:Mn^{II} ratio. For the **S60** and **S95** samples (2:3 initial ratio), $KMnO_4$ has totally reacted after 1 day of aging. For the **E60** and **E95** samples (20:3 initial ratio), a high consumption of $KMnO_4$ is observed (respectively, 73 and 99% of the initial quantity after 1 day of aging).

The mean average oxidation state (AOS) is 3.66 and confirms that birnessite has mixed valence (table 1). This value is consistent with previous reports of bulk birnessite synthesis through the sol−gel process[53,54] or solid state synthesis.[36] No significant variation of the *AOS* is observed whatever the synthesis conditions. The K:Mn ratio evaluated by elemental analysis is ca. 0.17. EDX analysis performed during FESEM observations is consistent with this value. The K:Mn content of the material is lower than previously reported values for sol−gel or solution based synthesis with usual values between 0.2 and 0.3.[38,53,54] Actually, two factors have to be considered. First, contrary to the method presented in this report, the reaction path for the sol−gel process toward bulk b-LMO does not involve the formation of layered

(65) JCPDS file 73−1604.

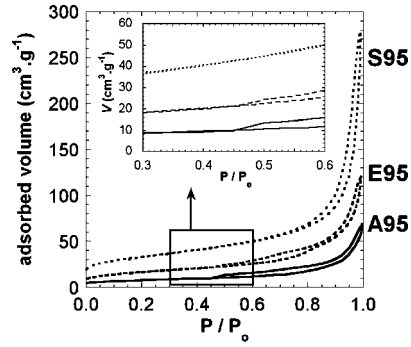

Figure 3. N_2 adsorption isotherms of b-LMO samples obtained after aging 7 days at 95 °C. Initial pH 11, 2:3 Mn^{VII}:Mn^{II} ratio (sample **S95**) (••••), initial pH 11, 20:3 Mn^{VII}:Mn^{II} ratio (sample **E95**) (---); initial pH 2, 20:3 Mn^{VII}:Mn^{II} ratio (sample **A95**) (—).

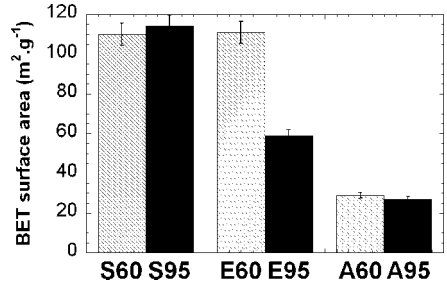

Figure 4. BET surface area of b-LMO samples obtained after aging 7 days at 60 °C (□) or 95 °C (■). Initial pH 11, 2:3 Mn^{VII}:Mn^{II} ratio (samples **S60** and **S95**); initial pH 11, 20:3 Mn^{VII}:Mn^{II} ratio (samples **E60** and **E95**); initial pH 2, 20:3 Mn^{VII}:Mn^{II} ratio (samples **A60** and **A95**).[30]

$Mn(OH)_2$.[53,54] The incorporation of K^+ is thus made easier in the sol−gel process because no diffusion of K^+ has to occur between previously formed octahedra layers. Second, the initial K:Mn ratio for reagents in the considered synthesis is ca. 1:1, contrary to previous reports of b-LMO synthesis through the solution route involving high initial K:Mn ratio (K:Mn > 3:1).[38] Thus the lower K:Mn content in the material described in this report could be due to the lower initial K:Mn ratio. Furthermore, the K^+ content is not sufficient to explain the low AOS and structural defects such as Mn^{4+} substitution by Mn^{3+}, with the negative charge of the oxygen framework compensated by the presence of hydroxo groups, must be invoked.[34−37]

To emphasize the feasibility of textural tayloring, a b-LMO material described previously[30] (sample **A95** obtained at initial pH 2, initial Mn^{VII}:Mn^{II} ratio 20:3 after aging 7 days at 95 °C) was compared to **S95** and **E95** samples. N_2 adsorption isotherms (Figure 3) show that samples obtained after aging 7 days at 95 °C have strongly different textural properties depending on the synthesis conditions. All samples exhibit type II adsorption isotherm.[66] The high adsorbed volume for sample **S95** is in agreement with the BET surface area (S_{BET}) of ca. 110 $m^2\ g^{-1}$ (Figure 4). By comparison, sample **A95** exhibits very low S_{BET} of 20 $m^2\ g^{-1}$. More generally, S_{BET} of samples synthesized at initial pH 11 (**S** and **E** samples) are much higher than those of samples obtained with initial pH 2 (**A** samples). An α-Plot analysis

(66) Sing, K. S. W.; Everett, D. H.; Haul, R. A. W.; Moscou, L.; Pierotti, R. A.; Rouquerol, J.; Siemieniewska, T. *Pure Appl. Chem.* **1985**, *57*, 603–619, IUPAC.

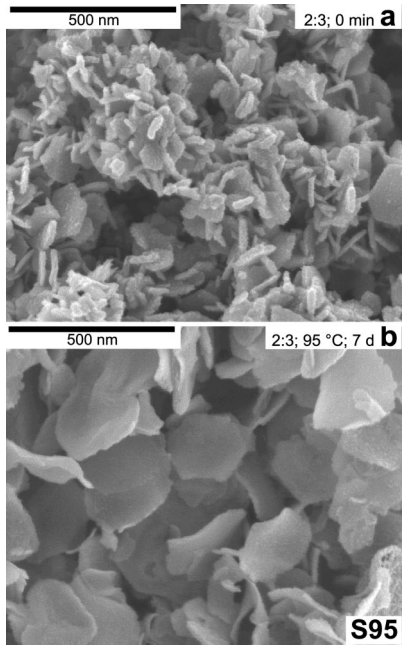

Figure 5. SEM micrographs of b-LMO samples obtained with the 2:3 Mn^{VII}:Mn^{II} ratio: (a) early precipitate and (b) after aging 7 days at 95 °C (sample **S95**).

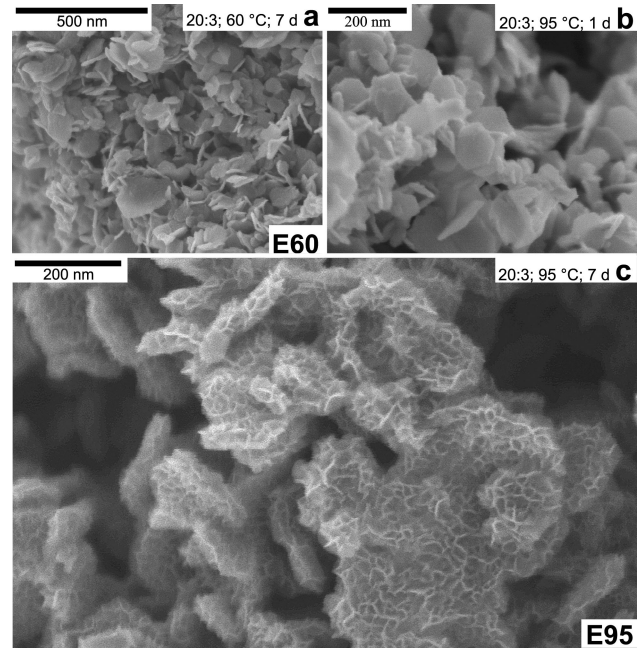

Figure 6. SEM micrographs of b-LMO samples obtained with the 20:3 Mn^{VII}:Mn^{II} ratio after aging (a) 7 days at 60 °C (sample **E60**), (b) 1 day at 95 °C, and (c) 7 days at 95 °C (sample **E95**).

of the adsorption branchs indicates the slit shape of the pores of all samples.[67] In parallel, the desorption branch of the isotherm of the sample **A95** exhibits a drop of the adsorbed volume at $p/p^{o} \approx 0.47$. Such a phenomenon is attributed to poorly accessible pores.[66] The same drop is observed for sample **E95**. Thus, the behavior of sample **E95** is intermediate between samples **S95** and **A95** in terms of specific area, pore shape, and accessibility. When aging at 60 °C for both ratios at initial pH 11 (samples **S60** and **E60**), textural properties are very similar to those of sample **S95** (Figure 4).

SEM micrographs show the different morphologies of the birnessite particles obtained immediately after mixing or after 1 or 7 days of aging, depending on the Mn^{VII}:Mn^{II} ratio and the temperature (Figures 5 and 6). Particles of the early precipitate obtained for both ratios are thin hexagonal sheets, of ca. 300 nm diameter and 10 nm thickness (Figure 5a). This bidimensional morphology is preserved upon aging for both ratios at both temperatures (**S** and **E** samples, Figures 5b, 6a, and 6c). Particles of the **E95** sample are thick platelets, with ca. 300 nm diameter and 30 nm thickness (Figure 6c). Moreover, careful examination indicates that the **E95** submicronic platelets exhibit a hierarchical architecture, with thin walls of ca. 10 nm width that have formed on the initial platelets, perpendicularly to the basal faces. The space between two walls in regard is ca. 50 nm.

TEM micrographs of the early precipitate for both ratios confirm the FESEM observations with hexagonal platelets of ca. 300 nm diameter and 10 nm thickness (Figures 7a and 8a). Lattice fringes with *d*-spacing of 0.42 nm observed by HRTEM along the edge of an early precipitate platelet (Figure 7c) does not match with the birnessite structure but fits the spacing between dehydrated layers as already reported.[30,37] Such shrinkage of the spacing between the MnO_6 layers is not observed on the XRD pattern and is

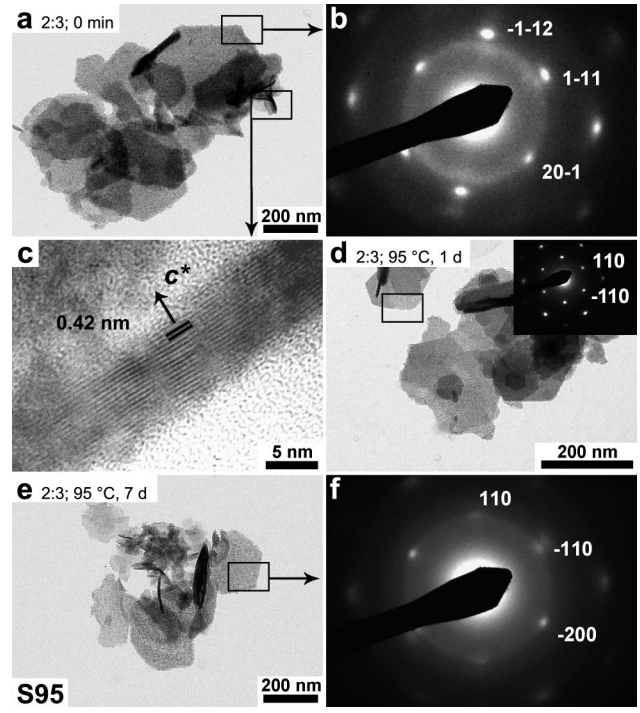

Figure 7. (a) TEM micrograph and (b) SAED pattern (zone axis [132]) of the early precipitated b-LMO obtained with the 2:3 ratio. HRTEM micrograph of the edge of an early platelet performed on an ultra thin section (c). TEM micrographs and SAED pattern (zone axis [001]) of the resulting b-LMO particles after aging at 95 °C for (d) 1 day and (e−f) 7 days ((e) sample **S95**, (f) zone axis [001]).

therefore attributed to dehydration under the electron beam, and fringes are indexed as the (001) layer planes of birnessite. SAED patterns of single particles of the early precipitates can be indexed in the *C*2/*m* space group of birnessite with

(67) Lippens, B. C.; Linsen, B. G.; de Boer, J. H. *J. Catal.* **1964**, *3*, 32–37.

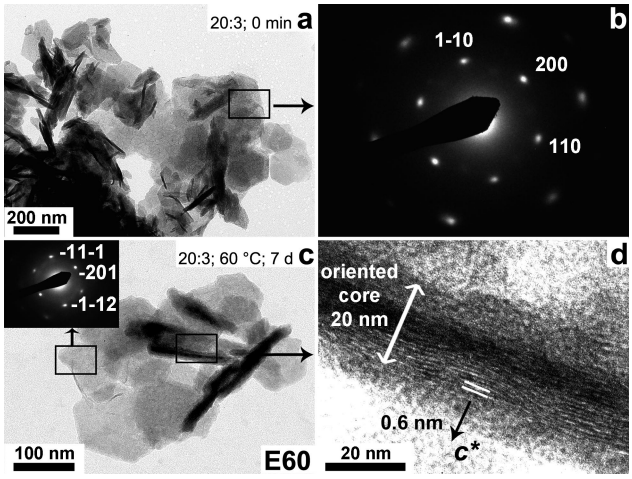

Figure 8. (a, b) TEM micrograph and SAED pattern (zone axis [001]) of the early precipitated b-LMO obtained with the 20:3 ratio. (c, d) TEM, HRTEM micrographs, and SAED pattern (zone axis [132]) of the resulting b-LMO particles obtained after aging 7 days at 60 °C (sample **E60**).

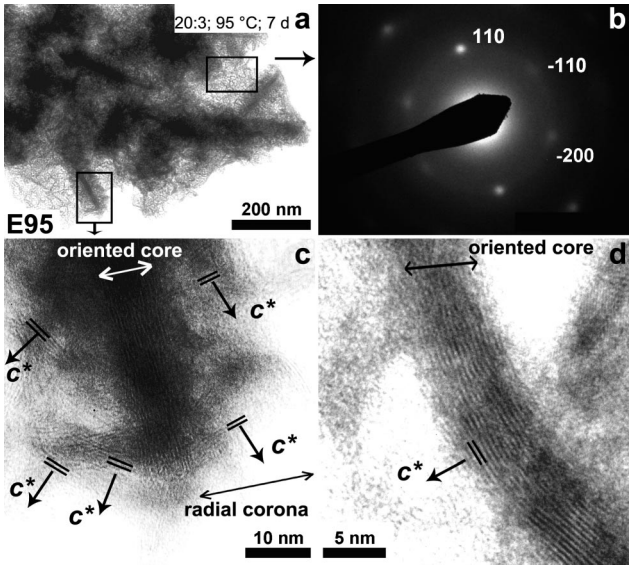

Figure 9. (a, b) TEM micrograph and SAED pattern (zone axis [001]) of b-LMO particles of sample **E95** obtained with the 20:3 ratio after aging 7 days at 95 °C. (c) HRTEM micrograph of the edge of a platelet exhibiting a radial corona. (d) HRTEM micrograph of the edge of a platelet performed on an ultra thin section, exhibiting a plateletlike core.

the [132] zone axis (Figures 7b, 8b).[32] This direction is close to ***c****, thus confirming that b-LMO is initially formed and that the early precipitates are identical, with (001) basal faces of the platelets in relation with the layered structure of both $Mn(OH)_2$ and birnessite. The platelet morphology is preserved upon aging at 60 °C (sample **S60**) and 95 °C (sample **S95**, panels e and f in Figure 7) for the 2:3 ratio and at 60 °C (sample **E60**, panels c and d in Figure 8) for the 20:3 ratio. The large width of the (001) XRD peak (Figure 2) is due to strains underlined by HRTEM micrographs with "curved" lattice fringes[34−37] and to the small thickness of the sheets. Consequently, the 20 nm thickness evaluated by TEM for **E60** sheetlike particles agrees with the distance range of ordered stacking between MnO_6 layers evaluated by XRD and confirms that basal faces are (001) planes. The very weak basal reflection of **S95** is due to both the smallest thickness of 10 nm (Figures 5b and 7c) and to a high concentration of defects which could be related to the lowest K+ content (Table 1).[34−36] Concerning sample **E95** obtained with the 20:3 ratio at 95 °C, examination of the edge of a platelet indicates a contrasted straight core (figure 9), characterized by a good alignment of the (001) fringes (Figure 9d) similar to the sheets observed for the 2:3 ratio (Figure 8d). Moreover, a less contrasted shell embedding the core is observed (Figure 9c). Once again, the shell exhibits (001) fringes. Within the corona, coherent domains have a diameter of ca. 10 nm and a different orientation than the core since no (001) fringe is observed parallel to the core. Therefore fringes observed in the shell correspond to the sponge-like architecture observed by FESEM, with thin 10 nm width vertical walls in respect to the sheetlike core. Thus, core−shell particles are obtained with a crystalline, oriented, platelet core and a shell made of thin crystalline vertical walls. By comparison, the **A95** sample exhibits a similar core−corona architecture, with a poorly ordered spherical core.[30]

Discussion

Aging Conditions. The high permanganate consumption observed for an excess of Mn^{VII} (20:3 ratio, samples **E60** and **E95**) in respect to the value of 18% expected from reaction 1 can be attributed to the metastability of permanganate aqueous solutions. In fact, MnO_4^- is a strong oxidizant ($E°_{25\ °C} = 1.70$ V/SHE) that is able to oxidize water ($E°_{25\ °C} = 1.23$ V/SHE) in relation to the following equation

$$4MnO_4^- + 2H_2O \rightarrow 4MnO_2 + 3O_2 + 4OH^- \qquad (2)$$

This reaction is fasten at high temperature (95 °C) and produces hydroxide ions. This explains the increase of basicity of the aging medium. Moreover, this second precipitation step does not involve Mn^{2+} and is much slower than the first reduction of MnO_4^- by Mn^{2+} (eq 1).

Shape and Structure Control. Mn^{2+} precipitates as the white solid $Mn(OH)_2$ above pH ∼8. Pyrochroite is rarely obtained as a pure compound since it is very sensitive to O_2 oxidation, which leads to brown haussmanite spinel Mn_3O_4.[68] Nevertheless, its TEM observation has already been reported, with submicrometric hexagonal platelet particles.[68] Such morphology is usual for many divalent hydroxides.[69] In the experimental procedure, at initial pH 11 (**S** and **E** samples), N_2 bubbling avoids fast oxidation of the early $Mn(OH)_2$ precipitate and preserves its plateletlike morphology before MnO_4^- addition. Highly basic medium preventing dissolution of the hydroxide and similarities between both lamellar structures ensure that the oxidation of $Mn(OH)_2$ by MnO_4^- occurs by a topotactic route, involving slight reorganization. Therefore, the sheet morphology is preserved upon phase transformation in the early step of the synthesis. The fast reduction of the MnO_4^- anions at the surface of the sheets leads to an epitaxial growth on the basal faces with strongly oriented sheets of birnessite (stage a of scheme **A**, Figure

(68) Bricker, O. *Am. Mineral.* **1965**, *50*, 1296–1354.
(69) Jolivet, J.-P. *Metal Oxide Chemistry and Synthesis. From Solution to Solid State*; Wiley: Chichester, U.K., 2000.

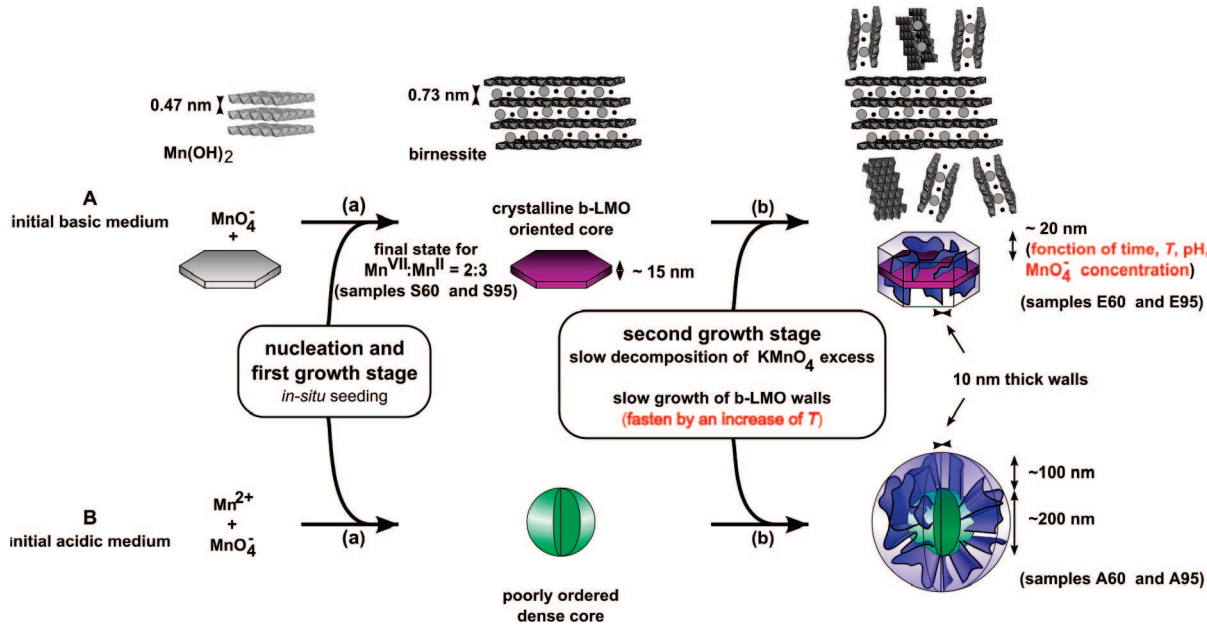

Figure 10. Reaction scheme of b-LMO formation. Route **A**: synthesis in initial basic medium of plateletlike hierarchical core-corona particles (samples **S60**, **S95**, **E60**, and **E95**). Route **B**: synthesis in initial acidic medium of ball-like hierarchical core−corona particles obtained previously (samples **A60** and **A95**).[30]

10). At the end of the nucleation step, an interesting parallel can be drawn between the formation mechanisms of nanosheets (samples **S** and **E**) and the spherical particles (samples **A**) described previously.[30] In both procedures, a fast reaction leads to an early particle during the first step of the synthesis. The structure of both early precipitates is related to birnessite, with already formed octahedra sheets. The final particle shape originates from the sheetlike or spherical morphology of the seed, which is governed by the initial pH. During the following shell growth stage, all samples evolve in basic medium where Mn^{II}, Mn^{III}, and Mn^{IV} species have very low solubility without any complexant, as deduced from the Pourbaix diagram ($[Mn^{2+}] = 2 \times 10^{-9}$ mol L^{-1} by considering the solubility of $Mn(OH)_2$ and an evolution pH of 12, whereas Mn^{3+} and Mn^{4+} concentrations are believed to be much lower for birnessite in aqueous medium).[70,71] This prevents the seeds from dissolution and ensures structure and shape preservation. Careful control of the evolution pH is therefore essential for the conservation of the seed as confirmed by Liu et al. who showed that b-LMO platelets are obtained by the MnO_4^-/Mn^{2+} reaction under hydrothermal conditions in a basic medium ([KOH] = 9 mol L^{-1}), whereas interestingly, the evolution in a more basic medium (ca. 13 mol L^{-1} KOH) increases the solubility of birnessite and leads to favored growth of b-LMO nanobelts by dissolution−crystallization.[58−60]

Morphology Control. Core−corona platelets are obtained for the initial $Mn^{VII}:Mn^{II}$ ratio 20:3. Slow reduction of the excess of MnO_4^- leads to slow growth of crystalline b-LMO thin walls around the initial sheets acting as seeds (stage b of scheme **A**, figure 10). As a result, during this slow second precipitation step following eq 2, a shell is formed around the initial platelets (sample **E95**). Poorly accessible pores obtained for $Mn^{VII}:Mn^{II} = 20:3$ at both initial pH (samples **A95** and **E95**) are located within the corona. The specific surface area of **E95** (60 m^2 g^{-1}) is higher than the one of **A95** (15 m^2 g^{-1}) and is related to the small thickness of **E95** corona, because of the initial smaller proton concentration (1×10^{-11} mol L^{-1} for **E95** compared to 1×10^{-2} mol L^{-1} for **A95**), which slows down reaction 2. Similarly, a shorter time of aging (1 day compared to 7 days for **E95**, Figure 6b) or a decrease in temperature inhibit the second step of precipitation and the shell formation (sample **E60** compared to **E95**). For stoichiometric ratio 2:3, after the in situ seeding stage, the soluble Mn^{VII} compound is no longer present in solution and available for the growth stage. The aged particles are then similar to the initial sheets (samples **S60** and **S95**). The lower specific area (15−60 m^2 g^{-1}) for core−corona particles (samples **A60**, **A95**, and **E95**) compared to sheetlike particles (110 m^2 g^{-1}) (samples **S60**, **S95**, and **E60**) is related to the corona, which gives corrugated sheets and less accessible pores, with an overall larger size (diameter or thickness) of the particles and a smaller N_2-probed surface. Moreover, the growth of the corona could lead to aggregation of particles, contributing to a decrease of the specific area. Finally, MnO_4^- concentration, aging time, temperature, and acidity enable fine control of the material architecture and resulting texture.

Conclusion

In conclusion, a low temperature (60 or 95 °C) procedure for aqueous precipitation of manganese oxide core−corona architectures has been developed. This environment friendly procedure is easily scaled up. The design of such hierarchical inorganic@inorganic particles is achieved by controlling the two kinetic pathways of the precipitation process. The first step has to be fast and to produce initial particles acting as seeds for the second, slower step of precipitation. The efficiency of such approach for morphological and textural tailoring is

stressed on by controlling (1) the initial acidity which governs the final particle shape and (2) the reactant ratio, aging time, temperature, and aging acidity, which rule the corona formation. This one-pot procedure could be applied to many other fully inorganic materials, providing versatile control of the particle shape and the material texture. Finally, texture tailoring could greatly enhance tuning of the exchange and electrochemical properties.

(70) Baes, C. F.; Mesmer, R. E. *The Hydrolysis of Cations*; Wiley: New York, 1976.
(71) Pourbaix, M. *Atlas d'Equilibres Electrochimiques*; Gauthier-Villars: Paris, 1963.

Acknowledgment. The authors thank Sophia Khan and Nathalie Bridonneau for experimental support; Dr. Patricia Beaunier (University of Paris 6), Dr. Dominique Jalabert, and Anny Richard (University of Orleans) for TEM, HRTEM, and FESEM observations; and Anny Anglo (University of Paris 6) for ultra thin sections.

CM801400B